Article

Mineralogical Constraints on Magma Recharge and Mixing of the Post-Collisional Potassic Volcanic Rocks in Dahongliutan, NW Tibetan Plateau

Wenjian Yang [1,2], Bo Zhao [1,2,*], Hongmei Yu [1,2], Jiandong Xu [1,2], Feixiang Wei [1,2] and Xiaoge Cui [3]

1   Jilin Changbaishan Volcano National Observation and Research Station, Institute of Geology, China Earthquake Administration, Beijing 100029, China; yangwenjian@ies.ac.cn (W.Y.); yuhongmei@ies.ac.cn (H.Y.); xujiandong@ies.ac.cn (J.X.); weifeixiang@ies.ac.cn (F.W.)
2   Key Laboratory of Seismic and Volcanic Hazards, China Earthquake Administration, Beijing 100029, China
3   Chongqing Vocational Institute of Engineering, Chongqing 402260, China; 18600213874@163.com
*   Correspondence: zhaobo@ies.ac.cn; Tel.: +86-136-9134-3483

Abstract: Post-collisional potassic magmatic rocks are widely distributed in the northwestern Tibetan Plateau, yet their magmatic processes remain poorly understood. Here, we present a comprehensive analysis of the whole-rock major and trace elements, as well as the mineral textures and chemistry of the Dahongliutan volcanic rocks in the NW Tibetan Plateau, aiming to reveal the magmatic processes prior to eruption and speculate on the triggering mechanism. The results show that the Dahongliutan volcanic rocks are potassic trachyandesites, which undergo polybaric crystallization during magma ascension. The phenocrysts in these potassic rocks exhibit various textural and compositional zoning styles. The green cores of green-core clinopyroxenes show textural (e.g., resorption texture) and chemical (Fe-rich) disequilibrium with the host rock compositions, suggesting that they may be antecrysts and crystallized from early batches of more evolved magmas. Additionally, alkali feldspar phenocrysts also display disequilibrium characteristics (e.g., overgrowth rim and sieve texture), indicating hot mafic magma recharge and mixing in the magma plumbing system. Therefore, we conclude that the disequilibrium textural and compositional features of green-core clinopyroxene and alkali feldspar phenocrysts provide evidence of magma recharge and mixing prior to eruption. Furthermore, it is likely that the eruption of the Dahongliutan volcano was triggered by magma recharge.

Keywords: zoning texture; magma recharge and mixing; Tibetan Plateau; Dahongliutan

1. Introduction

The injection of hot mafic magma into an evolved magma reservoir and subsequent magma mixing is not only considered as an important process causing the diversity of magma composition, but also a dominant eruption trigger for volcanoes [1–7]. Due to the fact that whole-rock compositions may represent the average of mineral phases and groundmass, they are unreliable for identifying open system processes of magmatic mixing. By contrast, minerals respond texturally and compositionally to changing magmatic environments, so they record a wealth of information concerning magmatic processes and composition in their crystal growth stratigraphy [8–12]. Therefore, detailed mineral-scale textural and chemical study can provide important clues to reconstruct magma plumbing processes (magma recharge and mixing) prior to eruption and offer petrological evidence for inferring the triggering mechanism of eruption [1,2,4,7,13,14].

With the closure of the Neo-Tethys ocean and collision of the India-Eurasia plate (55–65 Ma) [15,16], as well as the continuous northward subduction of the Indian plate, volcanic activity occurred across the whole process of uplift of the Tibetan Plateau, forming a series of large-scale volcanic rock belts (Figure 1a) [17,18]. Post-collisional potassic volcanic rocks, in

particular, have been thought to be an important window to explore the uplift process of the Tibetan Plateau and crust–mantle interaction [18–23]. It is noteworthy that the youngest post-collisional potassic rocks are mainly exposed in Western Kunlun in the northwestern Tibetan Plateau (Figure 1b). Numerous geochemical studies have demonstrated that these potassic rocks generally exhibit negative Nb, Ta and Ti anomalies, enrichment in incompatible elements and Sr-Nd-Pb isotopes, indicating the origin of an enriched lithospheric mantle [19,22–28]. Although previous studies have revealed their petrogenesis based on whole-rock compositions [29,30], in fact, many disequilibrium textures (e.g., the complex zoning of minerals) can be frequently observed and indicate a complex magmatic evolution history. For instance, when discussing magma mixing, if the hybrid members have similar isotopic compositions or insignificant differences in trace element concentrations, whole-rock data are less reliable than in situ data for minerals [31–34]. Hence, the in situ composition of minerals has a profound effect on identifying the magmatic processes (magma recharge and mixing) prior to eruption. Moreover, due to the extremely thick crust in the Tibetan Plateau, it makes the crustal magma evolution processes more complex. Here, we investigate the potassic volcanic rocks in Dahongliutan, NW Tibetan Plateau (Figure 1b), through a combined analysis involving whole-rock major and trace elements and petrography and mineralogy, to reveal the magma plumbing process and try to provide important information for the triggering mechanism of eruptions in the NW Tibetan Plateau.
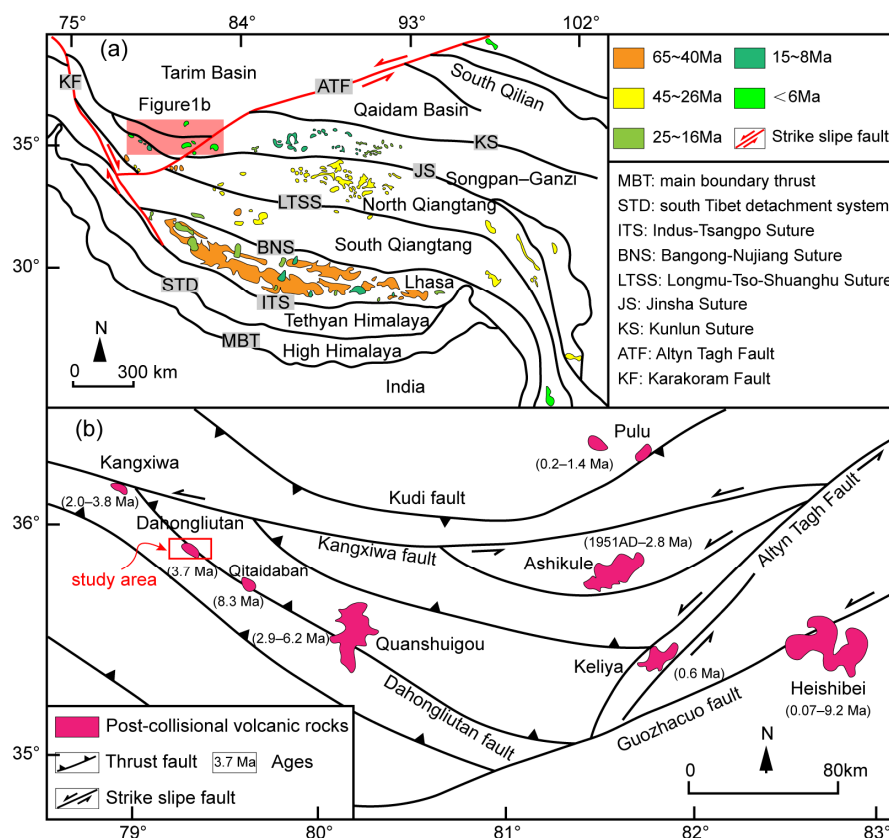

Figure 1. (**a**) Simplified map of the Tibetan Plateau showing the distribution of post-collisional volcanic rocks and major terranes (modified after [35]). The light red-filled rectangle shows the position of the Western Kunlun. (**b**) Geological sketch map showing the distribution of post-collisional volcanic rocks in Western Kunlun, NW Tibetan Plateau (modified after [22]).

2. Geological Setting and Samples

The Tibetan Plateau, situated in the eastern section of the Tethys-Himalayan tectonic domain, is formed by the combination of several continental terranes [36]. From south to north, these terranes are the Lhasa, Qiangtang, Songpan-Ganzi and Kunlun-Qaidam

terranes. They are separated by the Indus-Tsangpo, Bangong-Nujiang, Jinsha and Kunlun suture zones, respectively [37,38] (Figure 1a). These suture zones represent the relicts of the Neo-, Paleo- and Proto-Tethys oceans, respectively [39]. The heterogeneity of crustal thickness is one of the most notable characteristics of the Tibetan Plateau [40]. The crustal thickness under the Lhasa terrane can extend 70–80 km [41], while the crust beneath the Qiangtang and Songpan-Ganzi terrane is approximately 60 km thick [41,42]. Additionally, the plateau is widely distributed with a series of strike-slip faults, south-north normal faults and Cenozoic sedimentary basins [38,43]. Volcanic activity accompanied the entire evolution of the Tibetan Plateau from the Paleogene to the Quaternary [18,35,37], mainly consisting of post-collision potassium-rich volcanic rocks [18]. Among these rocks, the youngest post-collisional volcanic rocks are found in West Kunlun, NW Tibetan Plateau, with volcanic rock areas covering over 800 km^2. Currently, eight post-collisional potassic volcanic rock fields have been identified, including the Kangxiwa, Dahongliutan, Qitaidaban, Quanshuaigou, Pulu, Ashikule, Keliya and Heishibeihu fields, with ages ranging from 9.2 Ma to A.D. 1951 [22].

The Dahongliutan volcanic rock field is located 17 km east of the Dhongliutan service area (Hotan County, Xinjiang) along the G219 highway. It is on the NW-trending Dahongliutan fault zone along with the Kangxiwa, Qitaidaban and Qingshuigou volcanic rock fields. The Dahongliutan volcanic rock is exposed as a cliff on the south bank of the Karakashi River (Figure 2a), covering an area of 1 km^2. It stretches northwestward for approximately 0.5 km and has a thickness ranging from 5 to 30 m. The rock type is a series of potassic trachyandesites [22,27,28]. Previous studies have indicated two episodes of volcanic activity [44], but the volcanic stratigraphic profile does not show any noticeable discontinuity [17,45]. Furthermore, the latest SIMS zircon U-Pb ages from Dahongliutan trachyandesites range from 3.67 to 3.87 Ma [28], which is consistent with the age (3.7 Ma) determined by the high-precision ^{40}Ar/^{39}Ar stage heating method for feldspars [46], indicating that the volcanic activity age should be the Pliocene. In this study, ten lava samples were collected from the Dahongliutan volcanic field. These samples exhibit no significant signs of hydrothermal alteration or weathering and show a dark gray color with massive structures (Figure 2b). All volcanic samples display porphyritic textures, with phenocrysts of alkali feldspar, plagioclase, clinopyroxene, olivine, apatite and biotite. The groundmass contains plagioclase, alkali feldspar, clinopyroxene and Fe-Ti oxides (Figure 2c,d). More detailed petrographic characteristics and mineral compositions are provided in the following sections.

3. Analytical Methods

3.1. Whole-Rock Major and Trace Element Analyses

We selected well-cleaned fresh samples, crushed them into chips of 5 mm and removed altered grains, then ultrasonically cleaned with Milli-Q water and dried before they were powdered (200 mesh) using an agate mortar for whole-rock major and trace element analysis. Whole-rock major and trace elements were analyzed at Wuhan Sample Solution Analytical Technology Co., Ltd., Wuhan, China. Major elements were determined using a ZSX Primus II wavelength dispersive X-ray fluorescence spectrometer (XRF). The national standards GSR-2 and GSR-8 were used to monitor the analytical quality, and the analytical precision was better than 2% (Table S1). The trace elements were determined using an Agilent 7700e ICP-MS. The international reference standards AVG-2, BCR-2, BGM-2 and a blank sample were analyzed for quality, and the analytical precision for most trace elements was better than 5% (Table S1). Detailed analytical procedures have been described by [47].

3.2. In-Situ Major and Trace Element Analyses

Major element compositions of minerals were analyzed with a JEOL JXA-8230 electron probe microanalyzer (EPMA) at Wuhan Microbeam Analysis Technology Co., Ltd., Wuhan, China. The details of the EPMA methods are the same as those described by [48]. The beam diameter was set to 1 μm, and an acceleration voltage of 15 kV and a current of 20 nA were used for all analyses. Data were corrected online using the ZAF (Z, atomic number; A,

absorption; F, fluorescence) correction procedure. The peak counting time was 10 s for Na, Mg, Al, Si, K, Ca and Fe and 20 s for Ti and Mn. The upper and lower background counting time was half of the peak counting time. The following standards were used: sanidine (K), almandine (Fe and Al), diopside (Ca and Mg), jadeite (Na), rhodonite (Mn), olivine (Si) and rutile (Ti).
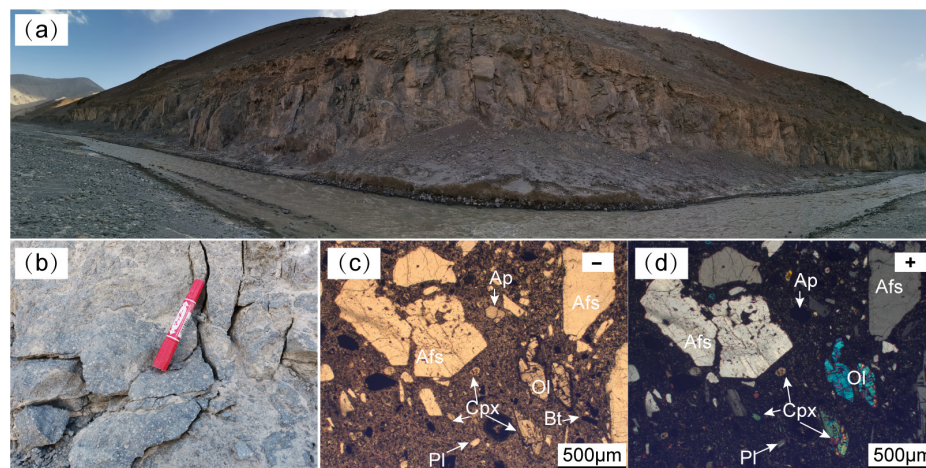

Figure 2. Representative field photographs and photomicrographs of the Dahongliutan volcanic rocks. (**a**) Field outcrop photograph; (**b**) Sample photograph; (**c,d**) Mineral assemblage (Afs + Ol + Cpx + Pl + Ap + Bt). Afs: alkali feldspar; Ol: olivine; Cpx; clinopyroxene; Pl: plagioclase; Ap: apatite; Bt: biotite. "+" and "−" indicate crossed and plane polarized light, respectively.

The trace element compositions of clinopyroxenes were analyzed by an Agilent 7700e LA-ICP-MS at Wuhan Sample Solution Analytical Technology Co., Ltd., Wuhan, China. The detailed operating conditions for the laser ablation system and the ICP-MS instrument and data reduction are the same as those described by [49]. Helium was applied as a carrier gas, and argon was used as an additional gas and mixed with the carrier gas via a T-connector prior to entering the ICP. The spot size, energy and frequency for this analysis were 44 μm, 80 mJ and 5 Hz, respectively. Each analysis included approximately 20–30 s of background acquisition followed by 50 s of data acquisition from the sample. Trace element compositions were calibrated against multiple reference materials (NIST610, BHVO-2G, BCR-2G and BIR-1G) without applying an internal standard. Off-line selection and integration of background and analyzed signals, time-drift correction and quantitative calibration were performed using ICPMSDataCal [47].

4. Results

4.1. Whole-Rock Major and Trace Elements

The results of major and trace elements are listed in Table S2. All samples display a low loss on ignition (LOI = −0.07–1.58 wt%), suggesting that they are almost unaffected by post-magmatic alteration. In the total alkali versus silica (TAS) diagram (Figure 3a), the Dahongliutan post-collisional volcanic rocks mainly consist of trachyandesites. These volcanic rocks show a relatively homogeneous composition, and their SiO_2 contents range from 55.35 to 58.67 wt%, MgO from 3.95 to 4.47 wt% and $Mg^{\#}$ [= molar $Mg^{2+}/(Mg^{2+} + Fe^{2+}) \times 100$, calculated assuming $Fe^{3+}/(Fe^{2+} + Fe^{3+}) = 0.10$ [50]] from 55.0 to 57.6. Furthermore, they show higher K_2O contents (4.80–5.11 wt%) relative to Na_2O (3.57–3.87 wt%), with K_2O/Na_2O ratios of 1.26–1.37. All the analyzed samples plot in the shoshonitic series (Figure 3b). In the Harker diagrams (Figure 4), the contents of MgO, CaO, MnO, TiO_2, $Fe_2O_3^T$ and P_2O_5 decrease with increasing SiO_2 content, and Al_2O_3, Na_2O and K_2O show a positive correlation with SiO_2, implying the fractional crystallization of olivine, clinopyroxene, feldspar and apatite.
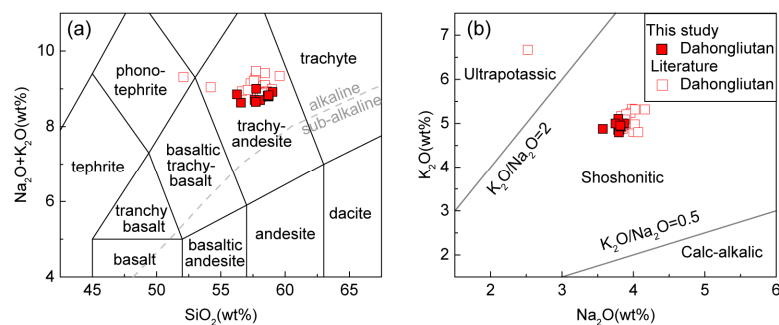
Figure 3. Classification diagram of the Dahongliutan post-collisional volcanic rocks. (**a**) Total alkali ($Na_2O + K_2O$) versus SiO_2 diagram (modified after [51]). (**b**) Na_2O (wt%) vs. K_2O (wt%). Literature data are from [27,28,46].
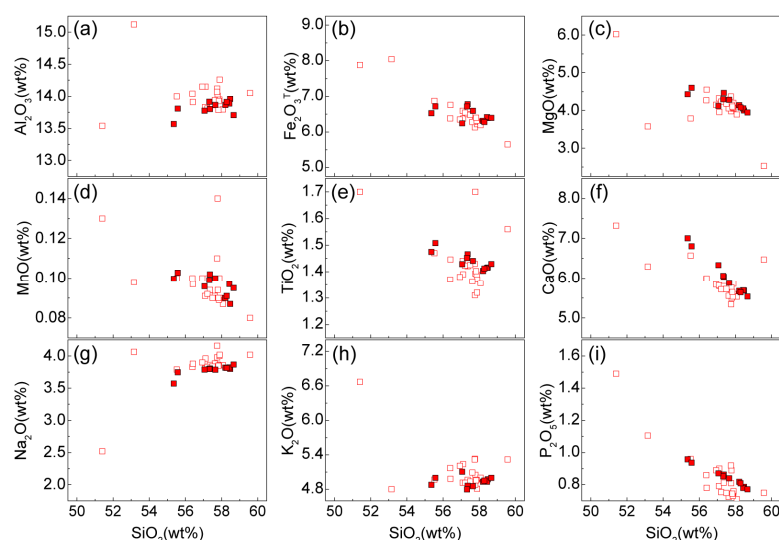

Figure 4. Harker diagram of Dahongliutan post-collisional volcanic rocks. Symbols are as in Figure 3.

On the primitive mantle-normalized trace element spider diagram (Figure 5a), the Dahongliutan post-collisional volcanic rocks are characterized by notable enrichment in large-ion lithophile elements (LILEs; e.g., Rb, Th, U and Pb) and by depletion in high-field-strength elements (HFSEs; e.g., Nb, Ta, Ti and P), typical of subduction-related magmatic rocks. On the chondrite-normalized rare earth element (REE) diagram (Figure 5b), they show a strong fractionation between LREEs and HREEs, with $(La/Yb)_N$ ratios of 68.0–98.2. In addition, all rocks are characterized by slightly negative Eu anomalies ($Eu/Eu^* = 0.81$–0.87).

4.2. Mineral Textures and Chemistry

4.2.1. Feldspar

Plagioclases and alkali feldspars are the most abundant minerals in Dahongliutan post-collisional potassic volcanic rocks. Alkali feldspars (10–15 vol.%) are not only the major phenocrysts, but also the main constituent mineral of the matrix. These phenocrysts show euhedral tabular shapes with sizes of 300–5000 μm, and some of them display Carlsbad twins, resorption and zoning textures (Figure 6a–c). Their compositions vary from sanidine ($Or_{51–58}Ab_{40–45}An_{1–4}$) to anorthoclase ($Or_{16–20}Ab_{63–68}An_{16–18}$) (Table S3, Figure 7a). Plagioclase phenocrysts (5 vol.%) display euhedral elongated shapes with sizes of 200–2000 μm. Their compositions vary from oligoclase ($Or_{10–11}Ab_{66–72}An_{19–22}$) to andesine ($Or_{4–6}Ab_{54–59}An_{36–42}$) (Table S3, Figure 7a).
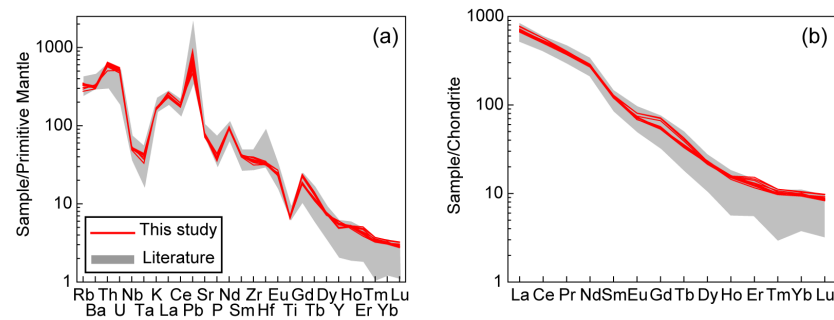
Figure 5. (**a**) Primitive mantle-normalized trace element spider diagram for Dahongliutan post-collisional volcanic rocks (normalizing values are from [52]); (**b**) Chondrite-normalized rare earth element diagram (normalizing values are from [53]). Literature data are from [27,28,46].
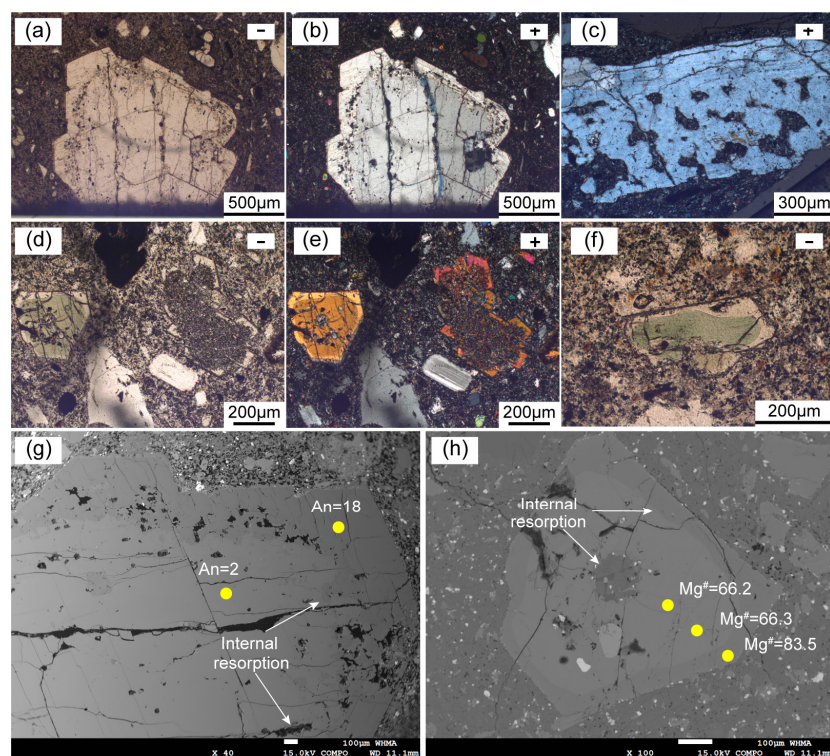
Figure 6. (**a**) Representative mineral textures and zoning photographs. (**a,b**) Alkali feldspars with overgrowth rim (reverse zoning); (**c**) sieve-textured alkali feldspar; (**d,e**) green-core clinopyroxene and strongly resorbed clinopyroxene; (**f**) green-core clinopyroxene; (**g**) and (**h**) are backscattered electron (BSE) images and composition profiles of reversely zoned alkali feldspar (**a**) and green-core clinopyroxene (**d**), respectively.
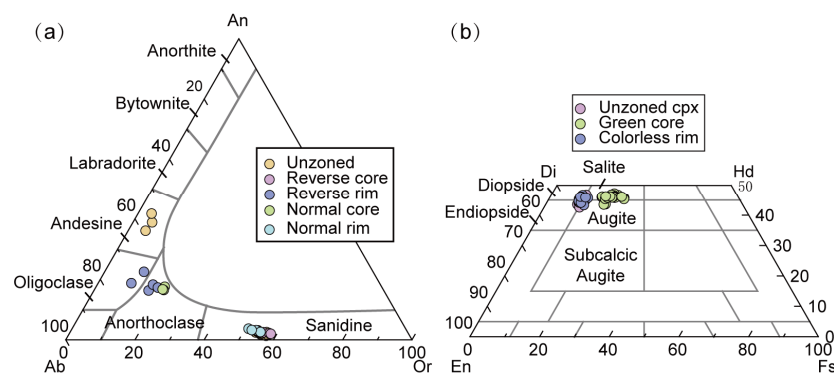
Figure 7. Classification diagram of (**a**) feldspar, and (**b**) Pyroxene (modified after [54]).

4.2.2. Clinopyroxene

Clinopyroxene is an important phenocryst and matrix mineral in Dahongliutan post-collisional potassic volcanic rocks. Clinopyroxene phenocrysts (~3 vol.%) show euhedral or subhedral columnar shapes with sizes of 300–3000 μm, and some phenocrysts display resorbed and zoning textures (Figure 6). Based on zoning features, two types of clinopyroxene phenocrysts have been identified: unzoned and reverse-zoned phenocrysts (Figure 7b). The major element results for clinopyroxenes are listed in Table S4. The unzoned clinopyroxene phenocrysts display narrow compositional ranges ($Wo_{43-47}En_{43-47}Fs_{9-10}$) with higher $Mg^{\#}$ values (81.6–84.5), consisting of augite, endiopside and diopside (Figure 7b). The reverse-zoning clinopyroxene phenocrysts with green cores (Figure 6a–d) are also known as "green-core clinopyroxene" [55,56]. The green cores are generally subcircular to subangular shapes, indicating partial resorption by the host melts. The green cores have distinctly higher contents of FeO (8.51–12.71 wt%), Na_2O (0.59–1.11 wt%) and MnO (0.23–0.49 wt%) and lower contents of MgO (11.23–13.75 wt%) and $Mg^{\#}$ (61.3–73.3) than their surrounding colorless rims (FeO: 5.29–7.81 wt%, Na_2O: 0.35–0.88 wt%, MnO: 0.05–0.20 wt%, MgO: 14.21–16.56 wt%, $Mg^{\#}$: 80.1–84.2) (Figure 8). The green cores are salite and augite in composition with $Wo_{43-47}En_{33-40}Fs_{15-22}$, whereas colorless rims consist of endiopside, diopside and augite in composition with $Wo_{43-47}En_{43-47}Fs_{9-11}$ (Figure 7a). Notably, these colorless rims show compositions similar to those of unzoned clinopyroxene (Figure 8). The results of trace elements for clinopyroxenes are presented in Table S5. The colorless rims of green-core clinopyroxenes display a lower ∑REE (89.14–135.57 ppm) compared to the green cores (234.90–437.68 ppm), but both exhibit LREEs enrichment relative to HREEs and slightly negative Eu anomalies (Eu/Eu* = 0.76–1.03) (Figure 9a). Moreover, the green cores and colorless rims show similar distribution patterns of trace elements (Figure 9b).

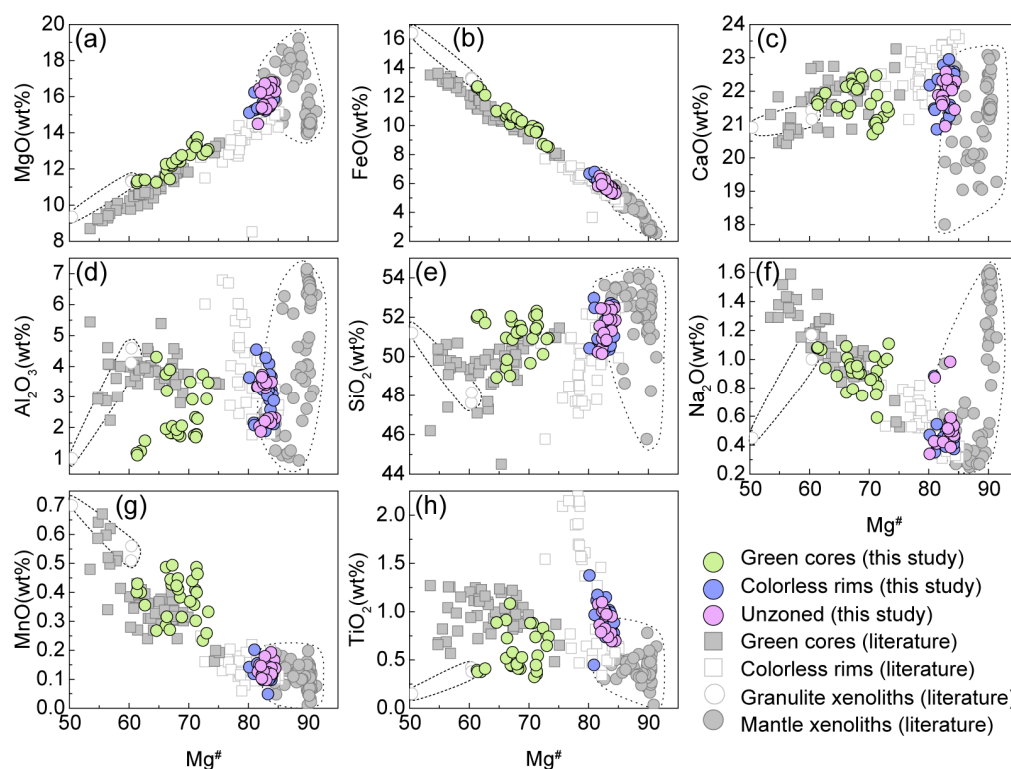**Figure 8.** Major element vs. $Mg^{\#}$ values in clinopyroxenes from Dahongliutan post-collisional rocks. Data sources are refs. [57,58] for clinopyroxenes in mantle xenoliths, ref. [59] for clinopyroxenes in granulite xenoliths and refs. [60–62] for green-core clinopyroxenes in post-collisional potassic volcanic rocks from North Tibet.
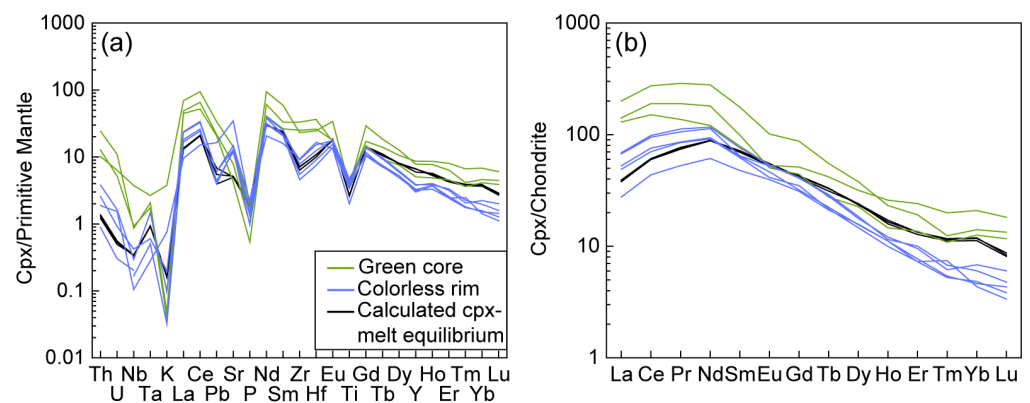
Figure 9. (**a**) Chondrite-normalized rare earth element diagram (normalizing values are from [53]); (**b**) Primitive mantle-normalized trace element spider diagram for clinopyroxenes in Dahongliutan post-collisional volcanic rocks (normalizing values are from [52]). Partition coefficients between clinopyroxene and melt of [63] are used to calculate the clinopyroxene compositions in equilibrium with host melts.

4.2.3. Olivine

Olivine grains (~1 vol.%) are euhedral or subhedral granular shapes with sizes of 300–1000 μm, and some have black (biotite) rims. They show a relatively narrow range of Fo content (79.8–85.3) (Table S6), consisting of chrysolites. Olivines from Dahongliutan post-collisional potassic rocks show relatively higher CaO contents (0.15–0.23 wt%) than mantle olivine xenocrysts (CaO < 0.1 wt%, [57,58,64]), which is consistent with a magmatic origin [65] rather than mantle xenocrysts.

4.2.4. Apatite

Apatite crystals are rare (~1 vol.%), but they have a clear surface and no inclusions, appearing as euhedral-subhedral columnar shapes with sizes of 200–2000 μm. Two crystals were selected for electron probe microanalysis (Table S7). The results show that the studied apatites are fluorapatites with F contents of 3.23–3.46 wt% and Cl contents of 0.44–0.47 wt%. The OH^- contents in apatites are 0.01–0.07 wt%, according to the calculation after [66].

5. Discussion

5.1. Mineral-Melt Equilibrium

Phenocrysts can either be in equilibrium with their host magma or not. When in equilibrium, these crystals are referred to as autocrysts and crystallize in situ from the host magma [12]. However, when in disequilibrium, these crystals are known as antecrysts or xenocrysts. Antecrysts are genetically related to the early batch of magmas and crystallize from the same magmatic system as autocrysts [8]. On the other hand, xenocrysts are accidentally captured wall rock or mantle xenoliths during magma ascent [12]. Furthermore, due to the high microcryst content in the matrix and the absence of usable melt inclusion compositions, we assume that the whole-rock composition is representative of the nominal host melt in equilibrium with phenocrysts [67,68].

The olivine-melt equilibrium is often tested using the Fe-Mg exchange coefficient (K_D $(Fe-Mg)^{ol-melt}$ = 0.30 ± 0.03) [69,70]. In the Rhodes diagram for olivines (Figure 10a), only a few olivines fall within the equilibrium field. However, most olivines fall above the equilibrium field, indicating that they are early crystallizing phenocrysts. Furthermore, some olivine phenocrysts exhibit black (biotite) rims (Figure 2c), indicating that they are not in equilibrium. For clinopyroxene, the equilibria is tested similarly to olivine-melt equilibria using K_D $(Fe-Mg)^{cpx-melt}$ = 0.275 ± 0.067 [68]. In the Rhodes diagram of clinopyroxenes (Figure 10b), the colorless rims of green-core clinopyroxenes and unzoned clinopyroxenes fall within the equilibrium field, suggesting that they are in equilibrium with the host potassic magmas. Therefore, these clinopyroxene rims are considered to be overgrowths

that crystallized in situ from the host potassic magmas. This is also supported by the similarities in REE and trace element distribution patterns between these colorless rims and the calculated clinopyroxene compositions in equilibrium with the host potassic magmas (Figure 9). However, the green cores have significantly lower $Mg^\#$ and plot below the equilibrium field, suggesting that they may be antecrysts and crystallized from earlier batches of more evolved magmas. Furthermore, the disequilibrium between green core and host magmas is also indicated by their subcircular to subangular shapes (Figure 6), suggesting partial resorption by the host potassic magmas.
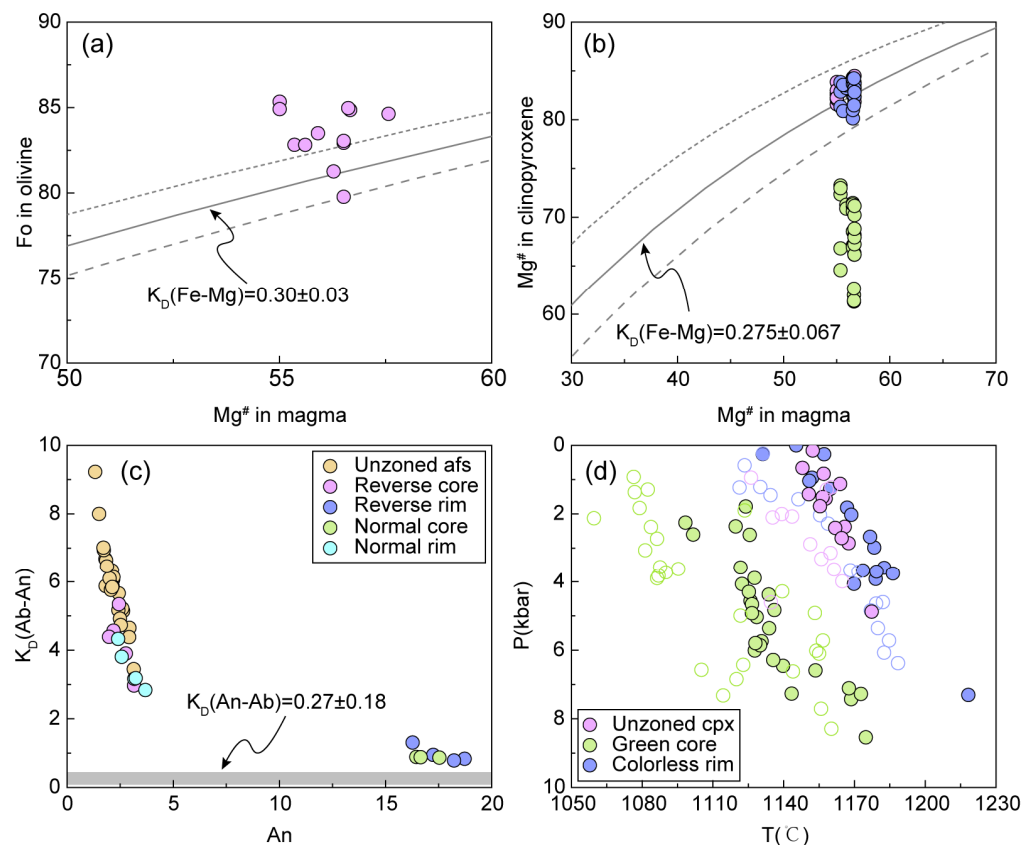

Figure 10. (**a**) Rhodes diagram of the olivine-melt equilibrium (K_D (Fe-Mg)$^{\text{ol-liq}}$ = 0.30 ± 0.03 [70]). (**b**) Rhodes diagram of the clinopyroxene-melt equilibrium (K_D (Fe-Mg)$^{\text{cpx-liq}}$ = 0.275 ± 0.067 [68]). (**c**) Testing diagram of the alkali feldspar-melt equilibrium (K_D (An-Ab)$^{\text{afs-liq}}$ = 0.27 ± 0.18 [69]). (**d**) Calculated temperatures and pressures of the crystallization of clinopyroxene phenocrysts. The solid circles represent the result of the calculation of the Wang model [71], the blank circles represent the results calculated by the Putirka model [69] for comparison.

For alkali feldspar, the equilibrium is tested using K_D (An-Ab)$^{\text{afs-melt}}$ = 0.27 ± 0.18 [69]. In Figure 10c, although almost all alkali feldspars plot above the equilibrium field, the lower An portions significantly exceed the equilibrium value. The decrease trend in the An value from core to rim in normal zoned feldspar phenocrysts is generally attributed to crystallization differentiation. Therefore, the An-poor rims are likely to be late crystallization products of more evolved magma. Considering that the composition of the rims of normal zoned feldspars is similar to the cores of reverse zoned feldspars, it is speculated that the An-poor cores may be antecrysts that crystallized from earlier batches of more evolved melts.

5.2. Crystallization Temperatures and Pressures

Clinopyroxene commonly occurs in mafic to intermediate rocks and exhibits various compositional variations. Therefore, the clinopyroxene-melt/clinopyroxene thermobarometer is frequently utilized to estimate the pre-eruptive temperatures, pressures and storage

depths of magma reservoirs [68,71–73]. However, it is crucial that the selected clinopyroxene is in equilibrium with the melt composition when using the clinopyroxene-melt thermobarometer. As discussed earlier, rims of green-core clinopyroxenes and unzoned clinopyroxenes are generally in equilibrium with host potassic magmas, while the green cores are not in equilibrium with host magmas. Therefore, in order to obtain reasonable temperature and pressure values and compare the relationship between the crystallization temperature and pressure of clinopyroxene with different compositions, the clinopyroxene-melt thermobarometer is not suitable for this study. Instead, we used the updated clinopyroxene-only thermobarometer [71], which is independent of melt compositions and solely relies on the composition of clinopyroxene. Furthermore, it provides a higher accuracy for pressure (± 1.7 kbar) and temperature (± 37 °C) estimation. For the sake of comparison, we performed additional calculations for the same samples based on Equations 32a and 32d [69].

The calculated crystallization temperatures and pressures of clinopyroxenes are presented in Table S4. The results of the two thermobarometers are consistent, indicating the reliability of the calculated values in this study. The crystallization temperatures and pressures for the green cores are 1098–1175 °C (1134 $\pm$ 18 °C) and 1.8–8.5 kbar (5.1 $\pm$ 1.7 kbar), respectively, and their surrounding rims are 1131–1218 °C (1169 $\pm$ 19 °C) and 0.0–4.1 kbar (2.5 $\pm$ 1.8 kbar), respectively. The temperature and pressure of the unzoned clinopyroxene are 1148–1177 °C (1160 $\pm$ 8 °C) and 0.1–4.9 kbar (1.9 $\pm$ 1.2 kbar), respectively. As shown in Figure 10d, there is a positive correlation between pressure and temperature, suggesting polybaric crystallization during magma ascension. Furthermore, we observe that the crystallization temperatures of the green cores are lower than their surrounding rims, while the colorless rims are comparable to the crystallization temperatures of the unzoned clinopyroxene. This is suggest that the green cores may have originated from a cooler, evolved magma, while the colorless rims and unzoned clinopyroxene may have originated from a hotter mafic magma.

5.3. Magma Recharge and Mixing Process

5.3.1. Constraints from Green-Core Clinopyroxenes

Green-core clinopyroxene is a reverse-zoned clinopyroxene phenocryst that consists of a green core and a colorless rim [55,56], which is also regarded as an important signal for an open system [12]. Green-core clinopyroxenes have been widely observed in alkaline mafic to intermediate-acidic volcanic rocks in various tectonic settings, such as cratons, continental rifts, orogenic belts and subduction zones [55,62,65,74–79]. However, the origin of green-core clinopyroxenes remains controversial. Two main hypotheses have been proposed: (1) the green cores could be xenocrysts [76,80,81], possibly derived from lower crustal granulite [76] or metasomatized lithospheric mantle [78,80,82]; (2) magma mixing between variably evolved magmas [6,56,65,79,83]. The green cores may represent antecrysts that crystallized from earlier batches of more evolved magmas, which later mixed with more primitive magmas.

Although green-core clinopyroxenes are commonly found in alkaline volcanic rocks, the minerals scraped from lower crustal granulite wall rocks or upper lithospheric mantle during the ascent of host magmas are accidental. In order to identify the origin of green-core clinopyroxenes in the Dahongliutan potassic rocks, we compared their major element contents with the compositions of clinopyroxene from mantle xenoliths [57,58], lower crust granulite xenoliths [59] and potassic rocks of northern Tibet [60–62]. Firstly, the compositions of the green core of green-core clinopyroxenes in the Dahongliutan potassic rocks are obviously distinct from those of clinopyroxenes in mantle peridotite and lower crustal granulite xenoliths (Figure 8), which rules out the possibility that the green cores originate from xenocrysts. Additionally, the green cores have significantly higher contents of FeO and Na_2O, but lower contents of MgO and $Mg^\#$, compared to their surrounding colorless rims (Figure 8). These characteristics eliminate the possibility of an origin through fractional crystallization in a closed system or crustal contamination in an open system during crystal growth, as these processes would result in normal zoning rather than

reverse-zoning clinopyroxene [32,84,85]. Furthermore, the similarity in the REE and trace element distribution patterns between the green cores and colorless rims of green-core clinopyroxenes (Figure 9) implies that the green cores and their surrounding colorless rims crystallized from co-genetic magmas. Moreover, the colorless rims of green-core clinopyroxenes are in equilibrium with the host potassic magmas (Figure 10b), indicating that these rims grew in situ from the current host magmas. These results are further supported by the similarities in the REE and trace element distribution patterns between colorless rims and the calculated clinopyroxene compositions in equilibrium with host magmas, using clinopyroxene-melt partition coefficients provided by [63] (Figure 9). Based on the K_D (Fe-Mg)$^{cpx-melt}$ value of 0.275 ± 0.067 [68], the estimated Mg$^{\#}$ values (24.8–48.4) of melts in equilibrium with green cores are lower than the Mg$^{\#}$ values (55.0–57.6) of host magmas (Figure 10b). This suggests that the green cores did not crystallize from the current host magma and may represent antecrysts that crystallized from earlier batches of more evolved melts. While clinopyroxene antecrysts are frequently invoked to explain the convection within the magmatic system or magma mixing, convection hardly causes significant differences in the core-rim composition of phenocrysts [85,86]. Additionally, the calculated crystallization temperatures of the green cores (1134 ± 18 °C) are lower than those of the colorless rims (1169 ± 19 °C), indicating the occurrence of hot magma recharge in the magma chamber. This finding is further supported by the presence of sieved and resorption textures in clinopyroxenes (Figure 6). In other words, clinopyroxene antecrysts are reheated due to the injection of hotter magma and resorption [34]. As the magmatic system tends towards equilibrium, reverse zoning (overgrowth rim) will form if antecrysts are not completely dissolved. Additionally, green-core clinopyroxenes with disequilibrium features have been observed in post-collisional potassic rocks from Bamaoqiongzong and Gemucuo, North Tibet [60–62], which have been interpreted as the result of mixing between variably evolved co-genetic magmas. It is noteworthy that both the green-core clinopyroxenes from Dahongliutan and North Tibet potassic rocks display similar major element variations (Figure 8), implying a consistent genesis. Therefore, we conclude that the green-core clinopyroxenes in the Dahongliutan potassic rocks are most likely formed through recharge mixing between a more evolved magma and a mafic magma. In other words, the green cores crystallized from a more evolved magma and subsequently mixed with a mafic magma, resulting in the development of Mg-rich rims (Figure 11).
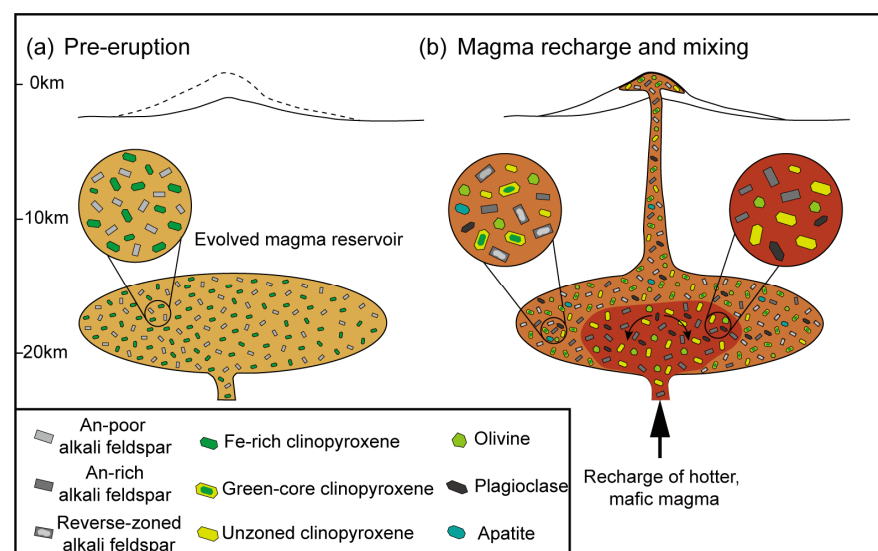

Figure 11. Schematic model of magma recharge and mixing in the magma plumbing system beneath the Dahongliutan volcano. (**a**) Prior to eruption, a more evolved magma reservoir beneath the Dahongliutan volcano. (**b**) The compositional zoning of phenocrysts was produced by a hotter mafic magma recharge and mixing process, which triggered the Dahongliutan volcano eruption.

5.3.2. Constraints from Reverse-Zoned Alkali Feldspars

Disequilibrium features of phenocrysts, including reverse zoning, resorption texture, a wide range of mineral compositions and minerals that are in disequilibrium with the host melt, are commonly regarded as evidence for magma recharge and mixing [7,87–89]. In this study, similar disequilibrium characteristics are observed in some feldspar phenocrysts in the Dahongliutan potassic rocks, suggesting a possible magma-mixing process. These feldspars display a wide range of compositions from $An_{1.3}$ to $An_{41.8}$, including andesine, oligoclase, anorthoclase and sanidine (Figure 7a). Some alkali feldspar phenocrysts exhibit obvious reverse zoning, indicating an open magmatic system [12]. While most reverse-zoned alkali feldspars plot above the equilibrium field (Figure 10c), the An-poor cores deviate further, implying that they may be antecrysts and crystallized from earlier batches of more evolved magmas. It is worth noting the presence of internal resorption textures in alkali feldspars, such as cellular textures and irregular cores of reverse-zoned alkali feldspars (Figure 6), which may record episodes of hot mafic magma recharge mixing [87]. Reverse zoning in feldspars is commonly attributed to the crystallization of a more Ca-rich melt, often associated with the mixing of a more mafic magma [12,88,90]. However, experimental studies have demonstrated that Ca-rich (An-rich) overgrowth rims can also form by increasing the temperature or pressure under H_2O-saturated conditions [91] or by elevating water activity [92]. Comparatively, temperature has a greater influence on inducing changes in the An value than pressure [12,91]. To further discriminate between these mechanisms, it is necessary to consider the variations An values and other elements (e.g., Fe, Mg, Ti and Ca) [93,94]. An increase in the An value coupled with an increase in the Fe content indicates magma mixing with Ca-rich magma, while a change in the An value without an increase in Fe mostly suggests a thermal or self-mixing process [14,93,95]. As shown in Table S3, the cores of the reverse-zoned alkali feldspars exhibit significantly lower An values (1.8–3.1), FeO (0.13–0.22 wt%) and CaO (0.36–0.64 wt%) contents compared to their surrounding rims (An: 16.3–22.5, FeO: 0.23–0.33 wt%, CaO: 3.41–4.72 wt%). Notably, the increase in the An value toward the rims of the reverse-zoned alkali feldspars is indeed accompanied by an increase in the FeO content, which cannot be solely explained by a single increase in temperature, pressure or H_2O activity [95], suggesting a more plausible scenario involving mixing with a hotter mafic magma (Figure 11).

5.4. Implications for Magmatic Eruptions

The recharge of mafic magma into an evolved magma reservoir is a widespread process in various volcanoes, including the Aeolian Islands [96], Tutupaca [13], Tungurahua [14], St Lucia [1], Changbaishan [97] and Tengchong volcanoes [98]. This recharge, along with the introduction of heat and volatiles, leads to dramatic changes in the temperature, pressure, viscosity and density of magma reservoirs. These changes result in rejuvenation and convection within the reservoir, ultimately triggering eruptions [1,4,5,13,14,99,100]. In the Dahongliutan post-collisional potassic volcanic rocks, the presence of reverse composition zoning and resorption textures in green-core clinopyroxene and alkali feldspar phenocrysts indicates mixing between a more evolved magma and a mafic magma. The cores of these phenocrysts represent the more evolved magma, while their rims correspond to a hotter mafic magma. Based on the above discussion, we propose a magma recharge and mixing model that explains the distinct textures and compositions of phenocrysts in the Dahongliutan post-collisional potassic volcanic rocks (Figure 11). Using the average pressures from the green cores of green-core clinopyroxenes, we estimate the depth of the pre-eruptive magma reservoir to be approximately 19 km (converted using a crustal density of 2.7 g/cm^3). Within this magma reservoir, extensive crystallization occurred, resulting in a crystal-rich mush containing Fe-rich clinopyroxene (corresponding to the core of green-core clinopyroxene) and An-poor alkali feldspar (sanidine) (Figure 11a). Subsequently, the injection of hotter mafic magma at the base of the crystal-rich mush led to mixing (Figure 11b). During this process, clinopyroxenes and alkali feldspars that crystallized early from the more evolved magmas were partially resorbed and subsequently overgrown

with Mg-rich and An-rich rims, respectively, due to dissolution residues. Additionally, the replenishment of hot mafic magma not only caused remobilization and convection within the reservoir but also increased the pressure, promoting magma ascent and ultimately triggering the eruption of the Dahongliutan volcano (Figure 11b).

6. Conclusions

In this study, we present whole-rock major and trace elements, as well as mineral textures and chemistry studies, for the Dahongliutan volcanic rocks in the NW Tibetan Plateau. The main conclusions are as follows:

(1) The post-collisional volcanic rocks in Dahongliutan are potassic trachyandesites, which underwent polybaric crystallization during magma ascension;

(2) The presence of Fe-rich green cores (antecrysts) and resorption textures in the green-core clinopyroxenes, as well as the disequilibrium characteristics of alkali feldspar (e.g., sieve texture and reverse zoning), indicating that the magma plumbing system beneath Dahongliutan experienced magma recharge and mixing;

(3) The hot mafic magma recharge may have been an important trigger for the Dahongliutan eruption.

References

1. Bezard, R.; Turner, S.; Davidson, J.; Schmitt, A.K.; Lindsay, J. Origin and evolution of silicic magmas in oceanic arcs; an in situ study from St Lucia, Lesser Antilles. *J. Petrol.* **2017**, *58*, 1279–1318. [CrossRef]
2. Churikova, T.G.; Ivanov, B.V.; Eichelberger, J.; Wörner, G.; Browne, B.; Izbekov, P. Major and trace element zoning in plagioclase from Kizimen Volcano (Kamchatka): Insights into magma-chamber processes. *J. Volcanol. Seismol.* **2013**, *7*, 112–130. [CrossRef]
3. Larsen, J.F.; Schaefer, J.; Vallance, J.W.; Neill, O.K. Petrology and geochemistry of three Early Holocene eruptions from Makushin Volcano, Alaska. *Bull. Volcanol.* **2020**, *82*, 72. [CrossRef]
4. Murphy, M.D.; Sparks, R.S.J.; Barclay, J.; Carroll, M.R.; Brewer, T.S. Remobilization of andesite magma by intrusion of mafic magma at the Soufriere Hills Volcano, Montserrat, West Indies. *J. Petrol.* **2000**, *41*, 21–42. [CrossRef]

5. Sparks, S.R.J.; Sigurdsson, H.; Wilson, L. Magma mixing: A mechanism for triggering acid explosive eruptions. *Nature* **1977**, *267*, 315–318. [CrossRef]

6. Yang, Z.; Hou, T.; Wang, D.; Marxer, F.; Wang, M.; Chebotarev, D.; Zhang, Z.; Zhang, H.; Botcharnikov, R.; Holtz, F. The role of magma mixing in the petrogenesis of eocene ultrapotassic lavas, Western Yunnan, SW China. *J. Petrol.* **2022**, *64*, egac129. [CrossRef]

7. Yu, H.; Xu, J.; Zhao, B.; Wei, F. Magmatic systems beneath Ashikule volcanic cluster (Western Kunlun, China): Insights from compositional and textural features of lavas. *Arab. J. Geosci.* **2020**, *13*. [CrossRef]

8. Davidson, J.P.; Morgan, D.J.; Charlier, B.L.A.; Harlou, R.; Hora, J.M. Microsampling and isotopic analysis of igneous rocks: Implications for the study of magmatic systems. *Annu. Rev. Earth Planet. Sci.* **2007**, *35*, 273–311. [CrossRef]

9. Ginibre, C.; Wörner, G.; Kronz, A. Crystal zoning as an archive for magma evolution. *Elements* **2007**, *3*, 261–266. [CrossRef]

10. Laurent, O.; Zeh, A.; Gerdes, A.; Villaros, A.; Gros, K.; Słaby, E. How do granitoid magmas mix with each other? Insights from textures, trace element and Sr–Nd isotopic composition of apatite and titanite from the Matok pluton (South Africa). *Contrib. Mineral. Petrol.* **2017**, *172*, 80. [CrossRef]

11. Rönick, R.; Renno, A. Clinopyroxene from basaltic rocks of the Erzgebirge-Krušné hory Mts.-implications for modelling the magmatic plumbing system. *J. Geosci.* **2012**, *55*, 231–249. [CrossRef]

12. Streck, M.J. Mineral textures and zoning as evidence for open system processes. *Rev. Mineral. Geochem.* **2008**, *69*, 595–622. [CrossRef]

13. Manrique, N.; Samaniego, P.; Médard, E.; Schiavi, F.; Mariño, J.; Liorzou, C. Pre-eruptive magmatic processes associated with the historical (218 ± 14 abp) explosive eruption of Tutupaca volcano (southern Peru). *Bull. Volcanol.* **2019**, *82*, 6. [CrossRef]

14. Samaniego, P.; Le Pennec, J.-L.; Robin, C.; Hidalgo, S. Petrological analysis of the pre-eruptive magmatic process prior to the 2006 explosive eruptions at Tungurahua volcano (Ecuador). *J. Volcanol. Geotherm. Res.* **2011**, *199*, 69–84. [CrossRef]

15. Cai, F.; Ding, L.; Yue, Y. Provenance analysis of upper Cretaceous strata in the Tethys Himalaya, southern Tibet: Implications for timing of India–Asia collision. *Earth Planet. Sci. Lett.* **2011**, *305*, 195–206. [CrossRef]

16. Ding, L.; Kapp, P.; Wan, X. Paleocene–Eocene record of ophiolite obduction and initial India-Asia collision, south central Tibet. *Tectonics* **2005**, *24*, TC3001. [CrossRef]

17. Deng, W. *Cenozoic Intraplate Volcanic Rocks in the Northern Qinghai-Xizang Plateau*; Geological Publishing House: Beijing, China, 1998.

18. Mo, X.; Zhao, Z.; Deng, J.; Flower, M.; Yu, X.; Luo, Z.; Li, Y.; Zhou, S.; Dong, G.; Zhu, D.; et al. Petrology and geochemistry of postcollisional volcanic rocks from the Tibetan Plateau: Implications for lithosphere heterogeneity and collision-induced asthenospheric mantle flow. In *Postcollisional Tectonics and Magmatism in the Mediterranean Region and Asia*; Dilek, Y., Pavlides, S., Eds.; Geological Society of America: Reston, VA, America, 2006; Volume 409, pp. 507–530.

19. Arnaud, N.O.; Vidal, P.; Tapponnier, P.; Matte, P.; Deng, W.M. The high K_2O volcanism of northwestern Tibet: Geochemistry and tectonic implications. *Earth Planet. Sci. Lett.* **1992**, *111*, 351–367. [CrossRef]

20. Guo, Z.; Wilson, M. Late Oligocene–early Miocene transformation of postcollisional magmatism in Tibet. *Geology* **2019**, *47*, 776–780. [CrossRef]

21. Guo, Z.; Wilson, M.; Liu, J.; Mao, Q. Post-collisional, potassic and ultrapotassic magmatism of the northern Tibetan Plateau: Constraints on characteristics of the mantle source, geodynamic setting and uplift mechanisms. *J. Petrol.* **2006**, *47*, 1177–1220. [CrossRef]

22. Guo, Z.; Wilson, M.; Zhang, L.; Zhang, M.; Cheng, Z.; Liu, J. The role of subduction channel mélanges and convergent subduction systems in the petrogenesis of post-collisional K-rich mafic magmatism in NW Tibet. *Lithos* **2014**, *198–199*, 184–201. [CrossRef]

23. Turner, S.; Arnaud, N.; Liu, J.; Rogers, N.; Hawkesworth, C.; Harris, N.; Kelley, S.; Van Calsteren, P.; Deng, W. Post-collision, shoshonitic volcanism on the Tibetan Plateau: Implications for convective thinning of the lithosphere and the source of ocean island basalts. *J. Petrol.* **1996**, *37*, 45–71. [CrossRef]

24. Turner, S.; Hawkesworth, C.; Liu, J.; Rogers, N.; Kelley, S.; van Calsteren, P. Timing of Tibetan uplift constrained by analysis of volcanic rocks. *Nature* **1993**, *364*, 50–54. [CrossRef]

25. Wang, P.; Zhao, G.; Han, Y.; Liu, Q.; Zhou, N.; Yao, J.; Li, J.; Li, Y. Post-collisional potassic rocks in Western Kunlun, NW Tibet Plateau: Insights into lateral variations in the crust-mantle structure beneath the India-Asia collision zone. *Lithos* **2020**, *370–371*, 105645. [CrossRef]

26. Wei, F.; Prytulak, J.; Xu, J.; Wei, W.; Hammond, J.O.S.; Zhao, B. The cause and source of melting for the most recent volcanism in Tibet: A combined geochemical and geophysical perspective. *Lithos* **2017**, *288–289*, 175–190. [CrossRef]

27. Zhang, Z.; Xiao, X.; Wang, J.; Wang, Y.; Kusky, T.M. Post-collisional Plio-Pleistocene shoshonitic volcanism in the western Kunlun Mountains, NW China: Geochemical constraints on mantle source characteristics and petrogenesis. *J. Asian Earth Sci.* **2008**, *31*, 379–403. [CrossRef]

28. Wang, J.; Wang, Q.; Ma, L.; Hu, W.-L.; Wang, J.; Belousova, E.; Tang, G.-J. Rapid recycling of subducted sediments in the subcontinental lithospheric mantle. *J. Petrol.* **2023**, *64*, egad056. [CrossRef]

29. Wei, F.; Prytulak, J.; Baker, E.B.; Xu, J.; Zhao, B. Identifying tethys oceanic fingerprint in post-collisional potassium-rich lavas in Tibet using thallium isotopes. *Chem. Geol.* **2022**, *607*, 121013. [CrossRef]

30. Yuan, Y.; Zhong, Y.; Guo, F.; Xia, B.; Zhang, Y. Geochemical and geochronological constraints on the genesis of pliocene post-collisional granite porphyry and shoshonite in Quanshuigou, western Kunlun Mountains, NW Qinghai–Tibet Plateau. *Int. Geol. Rev.* **2020**, *64*, 275–296. [CrossRef]

31. Francalanci, L.; Avanzinelli, R.; Nardini, I.; Tiepolo, M.; Davidson, J.P.; Vannucci, R. Crystal recycling in the steady-state system of the active Stromboli volcano: A 2.5-ka story inferred from in situ Sr-isotope and trace element data. *Contrib. Mineral. Petrol.* **2012**, *163*, 109–131. [CrossRef]

32. Liang, Y.; Deng, J.; Liu, X.; Wang, Q.; Qin, C.; Li, Y.; Yang, Y.; Zhou, M.; Jiang, J. Major and trace element, and Sr isotope compositions of clinopyroxene phenocrysts in mafic dykes on Jiaodong Peninsula, southeastern North Vhina Craton: Insights into magma mixing and source metasomatism. *Lithos* **2018**, *302–303*, 480–495. [CrossRef]

33. Tepley, F.J., III; Davidson, J.P.; Tilling, R.I.; Arth, J.G. Magma mixing, recharge and eruption histories recorded in plagioclase phenocrysts from El Chichón Volcano, Mexico. *J. Petrol.* **2000**, *41*, 1397–1411. [CrossRef]

34. Wei, X.; Zhang, Y.; Shi, X.-F.; Castillo, P.R.; Xu, Y.-G. Concurrent magma mixing and crystallization processes revealed by clinopyroxene macrocrysts from Lamont guyot lavas in NW Pacific. *Lithos* **2022**, *428–429*, 106833. [CrossRef]

35. Xia, L.; Li, X.; Ma, Z.; Xu, X.; Xia, Z. Cenozoic volcanism and tectonic evolution of the Tibetan Plateau. *Gondwana Res.* **2011**, *19*, 850–866. [CrossRef]

36. Tapponnier, P.; Xu, Z.Q.; Roger, F.; Meyer, B.; Arnaud, N.; Wittlinger, G.; Yang, J.S. Oblique stepwise rise and growth of the Tibet Plateau. *Science* **2001**, *294*, 1671–1677. [CrossRef]

37. Chung, S.; Chu, M.; Zhang, Y.; Xie, Y.; Lo, C.; Lee, T.; Lan, C.; Li, X.; Zhang, Q.; Wang, Y. Tibetan tectonic evolution inferred from spatial and temporal variations in post-collisional magmatism. *Earth-Sci. Rev.* **2005**, *68*, 173–196. [CrossRef]

38. Yin, A.; Harrison, T.M. Geologic evolution of the Himalayan-Tibetan Orogen. *Annu. Rev. Earth Planet. Sci.* **2000**, *28*, 211–280. [CrossRef]

39. Wu, F.; Wan, B.; Zhao, L.; Xiao, W.; Zhu, R. Tethyan geodynamics. *Acta Petrol. Sin.* **2020**, *36*, 1627–1674.

40. Li, Q.; Gao, R.; Lu, Z.; Guan, Y.; Zhang, J.; Li, P.; Wang, H.; He, R.; Karplus, M. The thickness and structural characteristics of the crust across Tibetan Plateau from active-sources seismic profiles. *Earthq. Sci.* **2009**, *22*, 21–31. [CrossRef]

41. Zhao, W.; Mechie, J.; Brown, L.D.; Guo, J.; Haines, S.; Hearn, T.; Klemperer, S.L.; Ma, Y.S.; Meissner, R.; Nelson, K.D.; et al. Crustal structure of central Tibet as derived from project INDEPTH wide-angle seismic data. *Geophys. J. Int.* **2001**, *145*, 486–498. [CrossRef]

42. Yuan, X.; Ni, J.; Kind, R.; Mechie, J.; Sandvol, E. Lithospheric and upper mantle structure of southern Tibet from a seismological passive source experiment. *J. Geophys. Res. Solid Earth* **1997**, *102*, 27491–27500. [CrossRef]

43. Blisniuk, P.M.; Hacker, B.R.; Glodny, J.; Ratschbacher, L.; Bi, S.; Wu, Z.; McWilliams, M.O.; Calvert, A. Normal faulting in central Tibet since at least 13.5 myr ago. *Nature* **2001**, *412*, 628–632. [CrossRef]

44. Pan, G.; Wang, P.; Xu, Y. *Cenozoic Tectonic Evolution of the Tibetan Platrau*; Geological Publishing House: Beijing, China, 1990.

45. Zhao, B.; Wei, F.; Yang, W.; Xu, J.; Cui, X. *Cenozoic Volcanism along Dahongliutan Fault in the West Kunlun Mountains, China: Implication from Distribution of Volcanic Rocks, Volcanic Geology, and Geochemistry*; Geological Society Special Publications: London, UK, 2021; Volume 510, pp. 147–158.

46. Yang, D. *The $^{40}Ar/^{39}Ar$ Geochronology and Geochemistry Research on Cenozoic Volcanic Rocks of Hoh Xil and Kunlun in the Northern Tibetan Plateau*; University of Chinese Academy of Science: Beijing, China, 2011.

47. Liu, Y.; Hu, Z.; Gao, S.; Günther, D.; Xu, J.; Gao, C.; Chen, H. In situ analysis of major and trace elements of anhydrous minerals by LA-ICP-MS without applying an internal standard. *Chem. Geol.* **2008**, *257*, 34–43. [CrossRef]

48. Yang, S.; Jiang, S.; Mao, Q.; Chen, Z.; Rao, C.; Li, X.; Li, W.; Yang, W.; He, P.; Li, X. Electron probe microanalysis in geosciences: Analytical procedures and recent advances. *At. Spectrosc.* **2022**, *43*, 186–200. [CrossRef]

49. Zong, K.; Klemd, R.; Yuan, Y.; He, Z.; Guo, J.; Shi, X.; Liu, Y.; Hu, Z.; Zhang, Z. The assembly of Rodinia: The correlation of early neoproterozoic (ca. 900 ma) high-grade metamorphism and continental arc formation in the southern Beishan Orogen, southern Central Asian Orogenic Belt (CAOB). *Precambrian Res.* **2017**, *290*, 32–48. [CrossRef]

50. Wang, X.-C.; Li, Z.-X.; Li, X.-H.; Li, J.; Liu, Y.; Long, W.-G.; Zhou, J.-B.; Wang, F. Temperature, pressure, and composition of the mantle source region of late Cenozoic basalts in Hainan island, SE Asia: A consequence of a young thermal mantle plume close to subduction zones? *J. Petrol.* **2011**, *53*, 177–233. [CrossRef]

51. Le Bas, M.J.; Le Maitre, R.W.; Streckeisen, A.; Zanettin, B. A chemical classification of volcanic rocks based on the total alkali-silica diagram. *J. Petrol.* **1986**, *27*, 745–750. [CrossRef]

52. Sun, S.S.; McDonough, W.F. *Chemical and Isotopic Systematics of Oceanic Basalts: Implications for Mantle Composition and Processes*; Geological Society Special Publications: London, UK, 1989; Volume 42, pp. 313–345.

53. McDonough, W.F.; Sun, S.S. The composition of the Earth. *Chem. Geol.* **1995**, *120*, 223–253. [CrossRef]

54. Morimoto, N. Nomenclature of pyroxenes. *Mineral. Petrol.* **1988**, *39*, 55–76. [CrossRef]

55. Dobosi, G.; Fodor, R.V. Magma fractionation, replenishment, and mixing as inferred from green-core clinopyroxenes in Pliocene basanite, southern Slovakia. *Lithos* **1992**, *28*, 133–150. [CrossRef]

56. Duda, A.; Schmincke, H.U. Polybaric differentiation of alkali basaltic magmas: Evidence from green-core clinopyroxenes (Eifel, FRG). *Contrib. Mineral. Petrol.* **1985**, *91*, 340–353. [CrossRef]

57. Liu, C.; Wu, F.; Chung, S.; Zhao, Z. Fragments of hot and metasomatized mantle lithosphere in middle Miocene ultrapotassic lavas, southern Tibet. *Geology* **2011**, *39*, 923–926. [CrossRef]

58. Tang, G.; Wyman, D.A.; Wang, Q.; Ma, L.; Dan, W.; Yang, Y.; Liu, X.; Chen, H. Links between continental subduction and generation of Cenozoic potassic–ultrapotassic rocks revealed by olivine oxygen isotopes: A case study from NW Tibet. *Contrib. Mineral. Petrol.* **2022**, *177*, 53. [CrossRef]

59. Lai, S.; Liu, C.; Yi, H. Geochemistry and petrogenesis of Cenozoic andesite-dacite associations from the Hoh Xil Region, Tibetan Plateau. *Int. Geol. Rev.* **2003**, *45*, 998–1019. [CrossRef]

60. Fan, L.; Chi, X.; Zhang, R.; Sun, W.; Wang, L.; Ning, W. Genesis of green-core clinopyroxenes in Gemucuo Oligocene alkaline potassic volcanic rocks from Qiangtang area, North Tibet: Replenishing-mixing process of magma. *Glob. Geol.* **2015**, *34*, 273–282.

61. Fan, L. *Geochemistry of the Cenozoic Bamaoqiongzong Volcanic Rocks in Qiangtang and Its Tectonic Evolution of Lithosphere*; Jilin University: Changchun, China, 2015.

62. Qi, Y.; Wang, Q.; Wei, G.-J.; Wyman, D.A.; Zhang, X.-Z.; Dan, W.; Zhang, L.; Yang, Y.-N. Post-collisional silica-undersaturated Bamaoqiongzong volcanic rocks from Northern Qiangtang: Indicators of the mantle heterogeneity and geodynamic evolution of Central Tibet. *J. Petrol.* **2022**, *64*, egac123. [CrossRef]

63. Williams, H.M.; Turner, S.P.; Pearce, J.A.; Kelley, S.P.; Harris, N.B.W. Nature of the source regions for post-collisional, potassic magmatism in southern and northern Tibet from geochemical variations and inverse trace element modelling. *J. Petrol.* **2004**, *45*, 555–607. [CrossRef]

64. Thompson, R.N.; Gibson, S.A. Transient high temperatures in mantle plume heads inferred from magnesian olivines in Phanerozoic picrites. *Nature* **2000**, *407*, 502–506. [CrossRef]

65. Xu, Y.; Huang, X.; Menzies, M.A.; Wang, R. Highly magnesian olivines and green-core clinopyroxenes in ultrapotassic lavas from western Yunnan, China: Evidence for a complex hybrid origin. *Eur. J. Mineral.* **2004**, *15*, 965–975. [CrossRef]

66. Li, W.; Chakraborty, S.; Nagashima, K.; Costa, F. Multicomponent diffusion of f, cl and oh in apatite with application to magma ascent rates. *Earth Planet. Sci. Lett.* **2020**, *550*, 116545. [CrossRef]

67. Lucci, F.; Carrasco-Núñez, G.; Rossetti, F.; Theye, T.; White, J.C.; Urbani, S.; Azizi, H.; Asahara, Y.; Giordano, G. Anatomy of the magmatic plumbing system of Los Humeros Caldera (Mexico): Implications for geothermal systems. *Solid Earth* **2020**, *11*, 125–159. [CrossRef]

68. Putirka, K.D.; Mikaelian, H.; Ryerson, F.; Shaw, H. New clinopyroxene-liquid thermobarometers for mafic, evolved, and volatile-bearing lava compositions, with applications to lavas from Tibet and the Snake River Plain, Idaho. *Am. Mineral.* **2003**, *88*, 1542–1554. [CrossRef]

69. Roeder, P.L.; Emslie, R.F. Olivine-liquid equilibrium. *Contrib. Mineral. Petrol.* **1970**, *29*, 275–289. [CrossRef]

70. Putirka, K.D. Thermometers and barometers for volcanic systems. *Rev. Mineral. Geochem.* **2008**, *69*, 61–120. [CrossRef]

71. Wang, X.; Hou, T.; Wang, M.; Zhang, C.; Zhang, Z.; Pan, R.; Marxer, F.; Zhang, H. A new clinopyroxene thermobarometer for mafic to intermediate magmatic systems. *Eur. J. Mineral.* **2021**, *33*, 621–637. [CrossRef]

72. Petrelli, M.; Caricchi, L.; Perugini, D. Machine learning thermo-barometry: Application to clinopyroxene-bearing magmas. *J. Geophys. Res. Solid Earth* **2020**, *125*, e2020JB020130. [CrossRef]

73. Putirka, K.; Johnson, M.; Kinzler, R.; Longhi, J.; Walker, D. Thermobarometry of mafic igneous rocks based on clinopyroxene-liquid equilibria, 0–30 kbar. *Contrib. Mineral. Petrol.* **1996**, *123*, 92–108. [CrossRef]

74. Barton, M.; Varekamp, J.C.; Van Bergen, M.J. Complex zoning of clinopyroxenes in the lavas of vulsini, latium, Italy: Evidence for magma mixing. *J. Volcanol. Geotherm. Res.* **1982**, *14*, 361–388. [CrossRef]

75. Geng, X.; Liang, Z.; Zhang, W.; Liu, Y.; Hu, Z.; Deng, L. Formation of green-core clinopyroxene in continental basalts through magmatic differentiation and crustal assimilation: Insights from in-situ trace element and Pb isotopic compositions. *Lithos* **2022**, *410–411*, 106587. [CrossRef]

76. Huang, X.L.; Niu, Y.; Xu, Y.G.; Chen, L.L.; Yang, Q.J. Mineralogical and geochemical constraints on the petrogenesis of post-collisional potassic and ultrapotassic rocks from Western Yunnan, SW China. *J. Petrol.* **2010**, *51*, 1617–1654. [CrossRef]

77. Jankovics, M.É.; Taracsák, Z.; Dobosi, G.; Embey-Isztin, A.; Batki, A.; Harangi, S.; Hauzenberger, C.A. Clinopyroxene with diverse origins in alkaline basalts from the western Pannonian Basin: Implications from trace element characteristics. *Lithos* **2016**, *262*, 120–134. [CrossRef]

78. Pilet, S.; Hernandez, J.; Villemant, B. Evidence for high silicic melt circulation and metasomatic events in the mantle beneath alkaline provinces: The Na–Fe-augitic green-core pyroxenes in the Ttertiary alkali basalts of the Cantal massif (French Massif Central). *Mineral. Petrol.* **2002**, *76*, 39–62. [CrossRef]

79. Ziem à Bidias, L.A.; Chauhan, H.; Mekala, R.M.; Rao, N.V.C. Green core clinopyroxenes from basanites of Petpenoun volcanoes, Noun Plain, Cameroon volcanic line: Chemistry and genesis. *Bull. Volcanol.* **2021**, *83*, 13. [CrossRef]

80. Barton, M.; van Bergen, M.J. Green clinopyroxenes and associated phases in a potassium-rich lava from the Leucite Hills, Wyoming. *Contrib. Mineral. Petrol.* **1981**, *77*, 101–114. [CrossRef]

81. Zhu, Y.; Ogasawara, Y. Clinopyroxene phenocrysts (with green salite cores) in trachybasalts: Implications for two magma chambers under the Kokchetav UHP massif, North Kazakhstan. *J. Asian Earth Sci.* **2004**, *22*, 517–527. [CrossRef]

82. Markl, G.; Marks, M.A.W.; Frost, B.R. On the controls of oxygen fugacity in the generation and crystallization of peralkaline melts. *J. Petrol.* **2010**, *51*, 1831–1847. [CrossRef]

83. Chen, P.; Fang, N.; Yuan, X. Geochemical insights from clinopyroxene phenocrysts into the magma evolution of an alkaline magmatic system from the Sanshui Basin, South China. *Minerals* **2021**, *11*, 1295. [CrossRef]

84. Dai, L.; Zhao, Z.; Zheng, Y.; Zhang, J. Source and magma mixing processes in continental subduction factory: Geochemical evidence from postcollisional mafic igneous rocks in the Dabie orogen. *Geochem. Geophys. Geosyst.* **2015**, *16*, 659–680. [CrossRef]

85. Li, X.; Zeng, Z.; Yang, H.; Zhao, Y.; Yin, X.; Wang, X.; Chen, S.; Qi, H.; Guo, K. Integrated major and trace element study of clinopyroxene in basic, intermediate and acidic volcanic rocks from the middle Okinawa Trough: Insights into petrogenesis and the influence of subduction component. *Lithos* **2020**, *352–353*, 105320. [CrossRef]

86. Svetov, S.; Chazhengina, S.; Stepanova, A. Geochemistry and texture of clinopyroxene phenocrysts from Paleoproterozoic picrobasalts, Karelian Craton, Fennoscandian Shield: Records of magma mixing processes. *Minerals* **2020**, *10*, 434. [CrossRef]

87. Browne, B.L.; Eichelberger, J.C.; Patino, L.C.; Vogel, T.A.; Uto, K.; Hoshizumi, H. Magma mingling as indicated by texture and Sr/Ba ratios of plagioclase phenocrysts from Unzen volcano, SW Japan. *J. Volcanol. Geotherm. Res.* **2006**, *154*, 103–116. [CrossRef]

88. Couch, S.; Sparks, R.S.J.; Carroll, M.R. Mineral disequilibrium in lavas explained by convective self-mixing in open magma chambers. *Nature* **2001**, *411*, 1037–1039. [CrossRef]

89. Samaniego, P.; Eissen, J.-P.; Le Pennec, J.-L.; Robin, C.; Hall, M.L.; Mothes, P.; Chavrit, D.; Cotten, J. Pre-eruptive physical conditions of EI Reventador volcano (Ecuador) inferred from the petrology of the 2002 and 2004–2005 eruptions. *J. Volcanol. Geotherm. Res.* **2008**, *176*, 82–93. [CrossRef]

90. Martel, C.; Radadi Ali, A.; Poussineau, S.; Gourgaud, A.; Pichavant, M. Basalt-inherited microlites in silicic magmas: Evidence from Mount Pelée (Martinique, French West Indies). *Geology* **2006**, *34*, 905–908. [CrossRef]

91. Rutherford, M.; Sigurdsson, H.; Carey, S.; Davis, A. The May 18, 1980, eruption of Mount St. Helens: 1. Melt composition and experimental phase equilibria. *J. Geophys. Res. Solid Earth* **1985**, *90*, 2929–2947. [CrossRef]

92. Holloway, J.R. Fluids in the evolution of granitic magmas: Consequences of finite CO_2 solubility. *Geol. Soc. Am. Bull.* **1976**, *87*, 1513–1518. [CrossRef]

93. Ruprecht, P.; Wörner, G. Variable regimes in magma systems documented in plagioclase zoning patterns: El Misti stratovolcano and Andahua monogenetic cones. *J. Volcanol. Geotherm. Res.* **2007**, *165*, 142–162. [CrossRef]

94. Triebold, S.; Kronz, A.; Wörner, G. Anorthite-calibrated backscattered electron profiles, trace elements, and growth textures in feldspars from the Teide–Pico Viejo volcanic complex (Tenerife). *J. Volcanol. Geotherm. Res.* **2006**, *154*, 117–130. [CrossRef]

95. Andújar, J.; Costa, F.; Scaillet, B. Storage conditions and eruptive dynamics of central versus flank eruptions in volcanic islands: The case of tenerife (Canary Islands, Spain). *J. Volcanol. Geotherm. Res.* **2013**, *260*, 62–79. [CrossRef]

96. Rossi, S.; Petrelli, M.; Morgavi, D.; Vetere, F.P.; Almeev, R.R.; Astbury, R.L.; Perugini, D. Role of magma mixing in the pre-eruptive dynamics of the aeolian islands volcanoes (Southern Tyrrhenian Sea, Italy). *Lithos* **2019**, *324–325*, 165–179. [CrossRef]

97. Yi, J.; Wang, P.; Shan, X.; Ventura, G.; Wu, C.; Guo, J.; Liu, P.; Li, J. Modeling the multi-level plumbing system of the Changbaishan caldera from geochemical, mineralogical, Sr-Nd isotopic and integrated geophysical data. *Geosci. Front.* **2021**, *12*, 101171. [CrossRef]

98. Hu, J.H.; Song, X.Y.; He, H.L.; Zheng, W.Q.; Yu, S.Y.; Chen, L.M.; Lai, C.K. Constraints of texture and composition of clinopyroxene phenocrysts of Holocene volcanic rocks on a magmatic plumbing system beneath Tengchong, SW China. *J. Asian Earth Sci.* **2018**, *154*, 342–353. [CrossRef]

99. Chen, Z.; Zeng, Z.; Wang, X.; Peng, X.; Zhang, Y.; Yin, X.; Chen, S.; Zhang, L.; Qi, H. Element and Sr isotope zoning in plagioclase in the dacites from the southwestern Okinawa Trough: Insights into magma mixing processes and time scales. *Lithos* **2020**, *376–377*, 105776. [CrossRef]

100. Chen, Z.; Tamehe, L.S.; Zhang, Y.; Chen, S.; Zeng, Z.; Yin, X.; Wang, X.; Qi, H.; Cai, M. Mafic magma recharge triggered eruption of a long-lived shallow silicic magma reservoir beneath a submarine volcano from the southwestern Okinawa Trough. *Lithos* **2023**, *452–453*, 107229. [CrossRef]